On the Impact of the Preparation Method on the Surface Basicity of Mg–Zr Mixed Oxide Catalysts for Tributyrin Transesterification

Abdallah I. M. Rabee [1] [iD]**, Jinesh C. Manayil [2], Mark A. Isaacs [2], Christopher M. A. Parlett [2]** [iD]**, Lee J. Durndell [2], Mohamed I. Zaki [1],*, Adam F. Lee [3],*** [iD] **and Karen Wilson [3],***

[1]   Chemistry Department, Faculty of Science, Minia University, El-Minia 61519, Egypt; aimoftah@mu.edu.eg
[2]   European Bioenergy Research Institute, School of Engineering and Applied Sciences, Aston University, Aston Triangle, B4 7ET Birmingham, UK; cmjinesh@gmail.com (J.C.M.); mark.isaacs@ucl.ac.uk (M.A.I.); c.parlett@aston.ac.uk (C.M.A.P.); l.j.durndell@uu.nl (L.J.D.)
[3]   School of Science, RMIT University, Melbourne, Victoria 3001, Australia
*   Correspondence: mizaki@mu.edu.eg (M.I.Z.); adam.lee2@rmit.edu.au (A.F.L.); karen.wilson2@rmit.edu.au (K.W.)

check for updates

Abstract: Mixed metal oxides are promising heterogeneous catalysts for biofuel production from lipids via alcoholysis, however, the impact of solid acidity and/or basicity on reactivity is comparatively poorly understood. Two systematically related families of $MgO–ZrO_2$ mixed oxide catalysts were therefore prepared by different synthetic routes to elucidate the impact of surface acid-base properties on catalytic performance in the transesterification of tributyrin with methanol. The resulting materials were characterized by TGA-MS, ICP-OES, N_2 porosimetry, XRD, TEM, XPS, DRIFTS, and CO_2-temperature-programmed desorption (TPD). $MgO–ZrO_2$ catalysts prepared by both non-aqueous impregnation and citric acid-mediated sol–gel routes exhibit excellent activity and stability. The citrate routes favor highly dispersed MgO and concomitant Lewis acid-base pair formation at the interface with zirconia. However, for both the citrate and impregnation routes, tributyrin transesterification occurs over a common, strongly basic MgO active site.

Keywords: solid base; MgO; transesterification; mixed oxide; biodiesel

1. Introduction

Mixed metal oxides are of significant academic and industrial interest due to their tunable acid-base and redox properties. Mixed alkaline earth and transition metal oxides are of particular interest due to their low production costs, and constitute the largest family of such heterogeneous catalysts [1]. Zirconium oxide (ZrO_2) is one such prominent metal oxide with amphoteric character [2–4], but which in pure form is catalytically inactive for transesterification under mild conditions [5] due to its weak basicity. Efforts to improve the base strength of ZrO_2 have focused on its modification by alkaline earth metals such as calcium [6–8] and magnesium [5,9–14]. Such doped zirconias often exhibit a higher surface area, base strength, and stability relative to the parent individual metal oxide components, with Mg–Zr mixed oxides being promising candidates for reactions including Knoevenagel condensation [9,13], furfural–acetone aldol condensation [12], transesterification [5,15], and reduction of carbonyl compounds [16]. In the case of aldol condensation, Sádaba et al. [12] defined two distinct active sites for MgO-rich Mg–Zr mixed oxides: Mg–O–Mg and Mg–O–Zr sites, with the latter being more reactive.

One application where alkaline earth metal oxides have shown much recent promise is the production of fatty acid methyl esters [17] (colloquially termed biodiesel) by the transesterification

of triglycerides from plant or algal bio-oils [18]. This reaction is particularly efficient over solid base catalysts such as MgO, which are well suited to high-purity oils which possess a low free fatty acid content. Unfortunately, real bio-oils typically contain a wide, and ill-defined distributions of triglycerides spanning C16–C20 with varying degrees of saturation [19–21], and so are difficult feedstocks with which to benchmark catalysts and establish quantitative structure-function relationships. However, few pure triglycerides are commercially available, and the direct analysis of long-chain representatives (i.e., without derivitization) by gas chromatography requires a programmable on-column injector. As a consequence, tributyrin (C4 unsaturated) has emerged as a simple model triglyceride, whose catalytic conversion, and the formation of di- and monoglyceride intermediates and final methyl butyrate product (Scheme 1), are amenable to conventional gas chromatographic analysis. In this context, Kozlowski et al. examined tributyrin transesterification with methanol over Mg–Zr mixed oxides, and attributed the activity to a synergy between MgO base sites and ZrO_2 amphoteric sites resulting in a new active site at the interface between the two oxides [5]. Secondary ion mass spectrometry [16] indicates preferential segregation of MgO in MgO–ZrO_2 catalysts. MgO has been widely studied for application in biodiesel production [22–28]. However, there are few reports on the application of Mg–Zr mixed oxides to triacyl glyceride transesterification, and the nature of active catalytic species in such systems is poorly established.
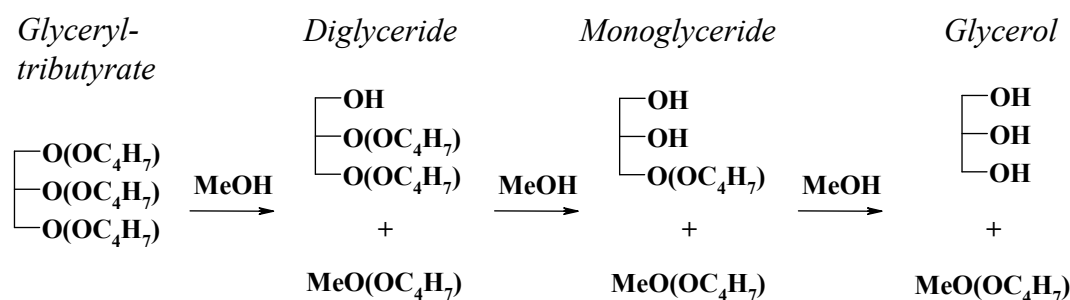
Scheme 1. Transesterification of glyceryl tributyrate in methanol to methyl butyrate.

Mg–Zr mixed oxides are most commonly prepared by co-precipitation [5,9–13], although alkoxide sol–gel [5,14] and wet impregnation methods [29] are also employed. The resulting mixed oxides usually exhibit large and inhomogeneous particle sizes, characterized by the presence of pure MgO and tetragonal ZrO_2 phases [5]. Such syntheses also require handling of hazardous alkoxide precursors and corrosive alkali reagents, and hence research has shifted to the development of greener preparative methods utilizing more environmentally benign chemicals. Citric acid [30] can be considered a biomass-derived carbohydrate and hence a more sustainable reagent for use as a chelating agent in sol–gel chemistry to prepare binary, ternary, and quaternary metal oxides with high degrees of homogeneity [31]. Citrate sol–gels employing metal nitrate precursors are also considered energy efficient syntheses wherein the nitrate acts as an oxidant and the citrate as fuel during the subsequent combustion [31].

Here we report the influence of the preparation method on the physicochemical and catalytic properties of Mg–Zr mixed oxides for tributyrin transesterification with methanol under mild conditions. Two families of Mg–Zr mixed oxides, containing similar MgO contents, were prepared via non-aqueous impregnation or citrate-mediated sol–gel processing.

2. Results and Discussion

2.1. Thermal Analysis

The thermal stability of dried Mg-Zr mixed oxides (MZ) precursors from both synthetic routes was explored by thermal analysis prior to calcination. Thermal gravimetric and differential thermal gravimetry (TGA/DTG) profiles for the 16.2 MZ precursor prepared by non-aqueous impregnation

of $Zr(OH)_4$ by $Mg(OCH_3)_2$ (Figure S1a) show three mass losses: (i) A slow loss of 13 wt % spanning from room temperature to 290 °C; (ii) a subsequent rapid and large loss of 10 wt % centered around 320 °C; and (iii) a final slow loss of ~3% that reaches a plateau beyond 700 °C. All these losses coincide with exothermic processes (Figure S1b), with mass spectrometry (MS) identifying that ≤290 °C as associated with loosely bound water molecules (Figure S1c), and a species with $m/z = 30$ (which reaches maximum desorption at 180 °C) likely associated with CH_2O fragments from the methoxide precursor. The rapid mass loss is accompanied by H_2O, CH_2O, CO_2, and $HCOOH$ desorption, and coincides with the temperature for $Zr(OH)_4$ decomposition to H_2O and ZrO_2 [32]. The total mass loss of 25.5% is slightly higher than that expected for the decomposition of pure $Zr(OH)_4$ into zirconia as expected because of the concomitant decomposition of $Mg(OCH_3)_2$ into MgO. The analogous 14.3 MZ precursor prepared by a citrate-mediated sol–gel undergoes a more significant mass loss (Figure S2a), losing 63% of its original mass by 560 °C, in three exothermic stages akin to the impregnated precursor (Figure S2b). Similar gas phase decomposition products were observed (Figure S2c), albeit over a wider temperature range extending up to 650 °C. In both synthetic routes, the formation of MgO_x and ZrO_x species appears to occur simultaneously, although citrate exhibits a higher thermal stability than methoxide/hydroxide.

2.2. Catalyst Characteristics

Structure and Composition

Inductively coupled plasma atomic emission spectroscopy (ICP-OES) and XPS analyses were employed to quantify the bulk and surface MgO content of MZ materials, respectively (Table S1). The surface Mg:Zr atomic ratio was higher than the corresponding bulk value in all cases, consistent with Mg surface segregation.

Figure 1a shows XRD patterns for pure zirconia (ZrO_2–HD) and xMZ–HD mixed oxide materials prepared by impregnation, where x is the MgO mass loading. ZrO_2–HD exhibited reflections corresponding to predominantly monoclinic (m-) ZrO_2 (JCPDS 86-1451 [33]), a minority tetragonal (t-) ZrO_2 phase (JCPDS 88-1007 [34]). In contrast, xMZ–HD only contained t-ZrO_2 crystallites for all MgO loadings (x = 2.1–18.2 wt %). Weak reflections characteristic of cubic (c-) MgO (labeled as ↓) were only observed for MgO loadings ≥6.34 wt %. Table 1 shows that t-ZrO_2 crystallites had smaller volume-averaged sizes (7.1–7.6 nm) than that observed for m-ZrO_2 (15.4 nm) in the pure ZrO_2–HD catalyst. Unlike ZrO_2–HD, the corresponding pure zirconia (ZrO_2–CT) analogue prepared by a citrate-mediated sol–gel route comprised predominantly t-ZrO_2. However, XRD patterns of the xMZ–CT analogues were qualitatively similar to those of the impregnated xMZ–HD family, containing only t-ZrO_2 crystallites and with c-MgO reflections emerging for loadings >8.7%. Average zirconia crystallite sizes for the xMZ–CT materials (4.5–6.5 nm) were likewise smaller than those observed for pure ZrO_2–CT (8.8 nm). The emergence of MgO features occurred at a slightly higher loading following the citrate-mediated synthesis, indicating that this route stabilizes more highly dispersed particles.
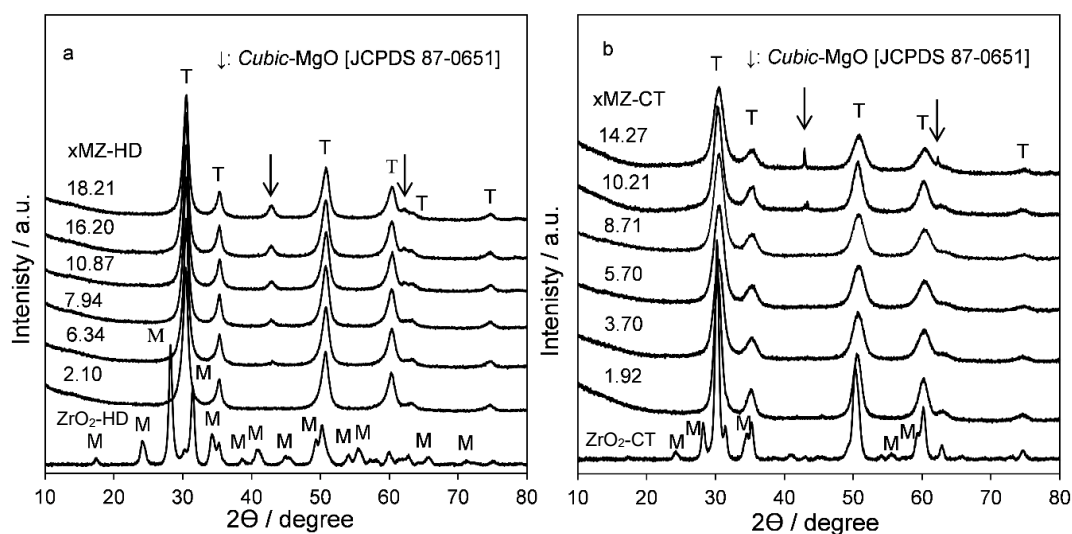
Figure 1. XRD patterns for: (**a**) xMZ–HD; and (**b**) xMZ–CT mixed oxides and corresponding pure zirconias.

Table 1. Physicochemical properties of xMZ–HD and xMZ–CT mixed oxides and corresponding pure zirconias.

Sample	S_{BET} [a]/$m^2 g^{-1}$	Crystallite Size [b]/nm	Basicity [c]/μmol·g^{-1}
ZrO₂-HD	59	15.4	11.7
2.1MZ–HD	152	7.2	32.7
6.3MZ–HD	190	7.3	44.0
7.9MZ–HD	129	7.6	47.8
10.9MZ–HD	137	7.5	69.8
16.2MZ–HD	149	7.4	72.9
18.2MZ–HD	140	7.1	94.8
ZrO₂-CT	50	8.8	4.9
1.9MZ–CT	87	6.5	7.3
3.7MZ–CT	114	4.8	9.8
5.7MZ–CT	125	4.4	13.9
8.7MZ–CT	107	4.4	23.8
10.2MZ–CT	105	4.4	37.6
14.3MZ–CT	117	4.6	35.0

[a] N₂ porosimetry; [b] ZrO₂ determined by Scherer equation; [c] CO₂-temperature-programmed desorption (TPD) analysis.

Transmission electron microscopy (TEM) images of the 7.9MZ–HD, 18.2MZ–HD, 8.7MZ–CT and 14.3MZ–CT samples are shown in Figure 2. All materials exhibited spherical morphologies with average particle diameters ranging from 5 to 10 nm (Figure 2e,h inset) in accordance with XRD, and (101) and (002) facets of t-ZrO₂ (Figure 2f–i). Brunauer-Emmett-Teller (BET) surface areas of xMZ–CT materials were systematically smaller than those of their xMZ–HD counterparts. Since the MZ–CT catalysts all exhibited smaller crystallite sizes than their MZ–HD counterparts (Table 1), the lower areas of the former must therefore be linked to a loss of interparticle voids (formation of larger agglomerates) which in turn restricts the accessible area that can be titrated by nitrogen. This hypothesis is supported by TEM which shows that 8.7MZ–CT (Figure 2a) formed denser agglomerates than 7.9MZ–HD (Figure 2g), and likewise for 14.3 MZ–CT (Figure 2k) versus 18.2MZ–HD (Figure 2e).

The surface chemical environment of both mixed oxide families was subsequently explored by X-ray photoelectron spectroscopy (XPS) (Figures S3–S5). Mg 2s XP spectra for xMZ–HD and xMZ–CT samples exhibited a single feature with a binding energy of approximately 88.3 eV in all cases indicative of a common MgO chemical environment [35]. Corresponding Zr 3d XP spectra also evidenced a

common zirconium chemical environment for all MgO loadings (Figure 3 and Figure S4). O 1s XP spectra were qualitatively similar for xMZ–HD and xMZ–CT families (Figure S5) evidencing two surface oxygen environments assigned to lattice oxygen (~529 eV) and hydroxyl and/or CO_x species (~531 eV). In both families, lattice oxygen appeared at a lower binding energy than observed for pure zirconia indicating a higher electron density and hence basicity [36].
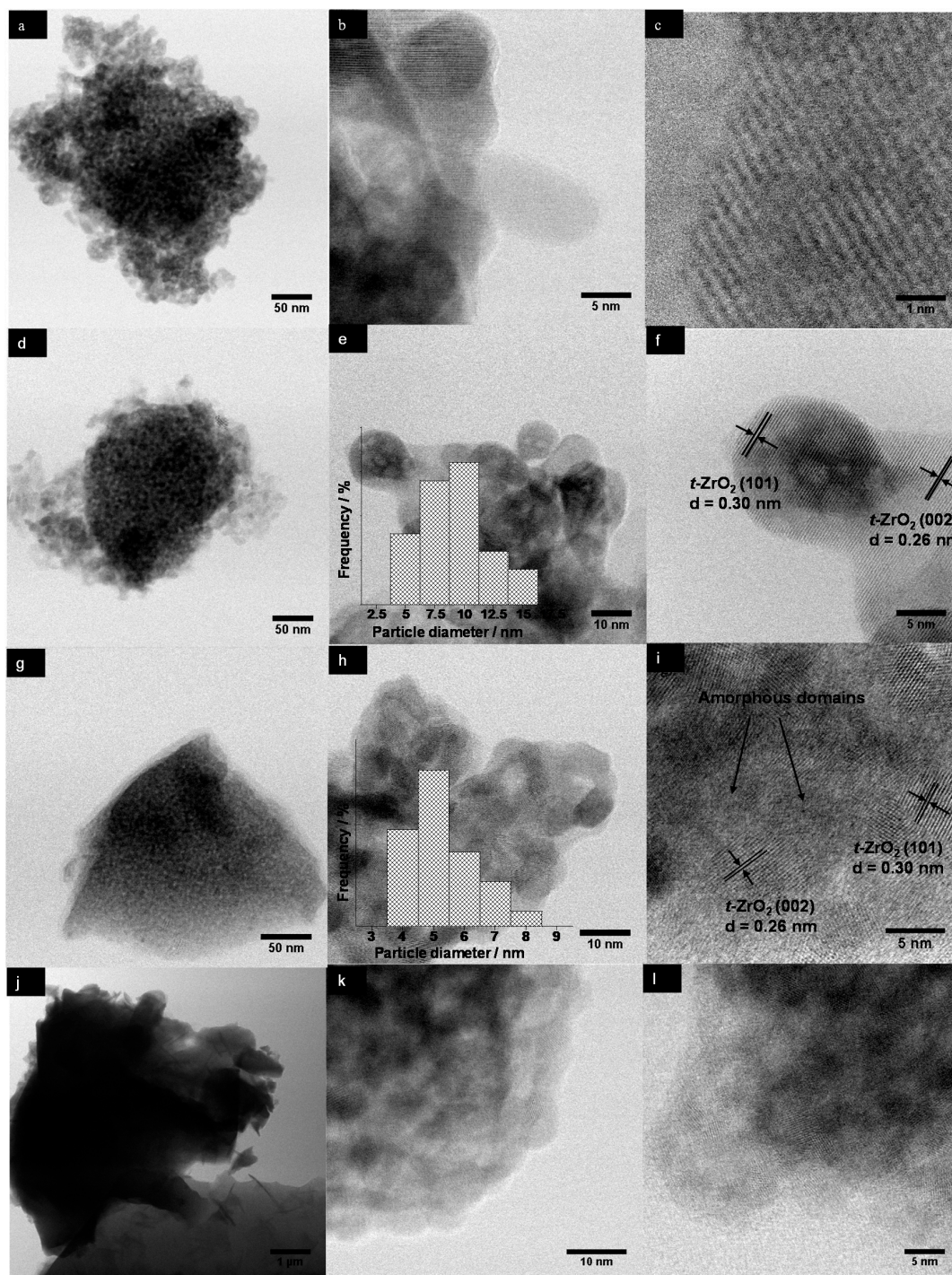

Figure 2. TEM and HRTEM images for: (**a**–**c**) 7.9MZ–HD; (**d**–**f**),18.2MZ–HD; (**g**–**i**) 8.7MZ–CT; and (**j**–**l**) 14.3MZ–CT catalysts, with particle size distributions inset for 18.21MZ–HD and 8.71MZ–CT.
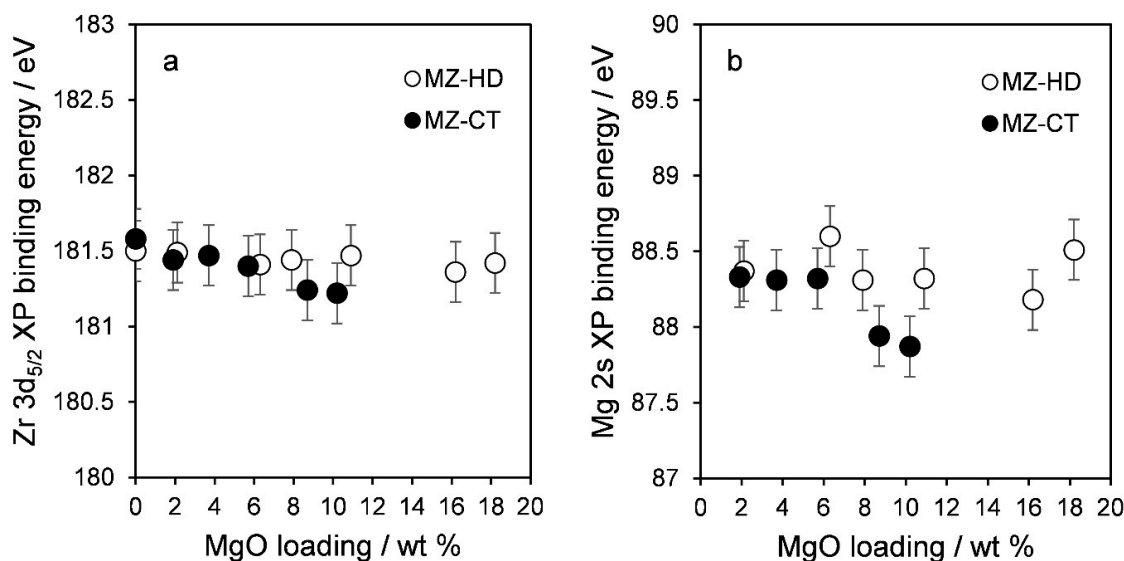
Figure 3. (**a**) Zr 3d; and (**b**) Mg 2s XP binding energies for xMZ–HD and xMZ–CT mixed oxides and corresponding pure zirconias.

Figure 4 compares diffuse reflectance infrared Fourier transform (DRIFT) spectra for both families following subtraction of their associated parent zirconia (uncorrected spectra are shown in Figure S6). Seven bands are observed for xMZ–HD materials at 1100, 1255, 1420, 1509, 1700, 3673, and 3720 cm^{-1}. The bands at 1255 and 1700 cm^{-1} are assigned to surface bicarbonate (species I in Scheme 2) [37], formed by atmospheric CO_2 interaction with surface hydroxyls. The bands at 1420 and 1509 cm^{-1} are assigned to $\nu_3 OCO$ vibrations of surface carbonate [38,39], whose splitting value ($\Delta\nu_3$) is indicative of the nature of base sites: $\Delta\nu_3$ ~100 cm^{-1} is representative of monodentate carbonate; chelating bidentate carbonate exhibit $\Delta\nu_3 < 250$ cm^{-1}; and bridged bidentate carbonate typically exhibit $\Delta\nu_3 > 250$ cm^{-1} [38]. This band splitting is also proposed to be a function of the surface partial charge in metal oxides, with smaller $\Delta\nu_3$ associated with stronger basic adsorption sites [39]. Accordingly, the present $\Delta\nu_3$ value of 89 cm^{-1} is consistent with monodentate carbonate (species II in Scheme 2) [40]. Since the relative intensity of hydroxyl bands gradually *increases* with MgO *content*, the band at 3700 cm^{-1} is most likely due to OH groups on MgO [39], whereas the band at 3673 cm^{-1} may arise from bridging hydroxyls (Zr–OH–Mg). Corresponding DRIFT spectra for xMZ–CT samples are shown in Figure 4b (uncorrected spectra are shown in Figure S6b) and exhibit a similar set of carbonate bands at 1088, 1195, 1385, 1537, and 1660 cm^{-1}. The middle set of bands with a $\Delta\nu_3$ splitting of 152 cm^{-1} are indicative of chelating bidentate carbonate (species III, Scheme 2) [38]. This splitting decreases with increasing MgO loading, suggesting either the formation of strong basic sites, likely associated with phase separated MgO particles observed by XRD, or a switch to monodentate carbonate. Only one hydroxyl band was observed for all xMZ–CT samples, shifting from 3620 cm^{-1} to 3668 cm^{-1} with increasing MgO, again consistent with the emergence of strongly basic pure MgO characteristics. Monodentate carbonate is favored over electron-rich surface oxides [41,42], whereas, chelating and bridging bidentate carbonates are favored by exposed M^{n+}-O^{2-} pairs of medium base strength [41–43]. Accordingly, DRIFTS suggest that the xMZ–HD samples are strong bases, while xMZ–CT samples are moderately basic at low MgO loading, becoming stronger bases due to MgO particle growth $\geq$8.71 wt % MgO.
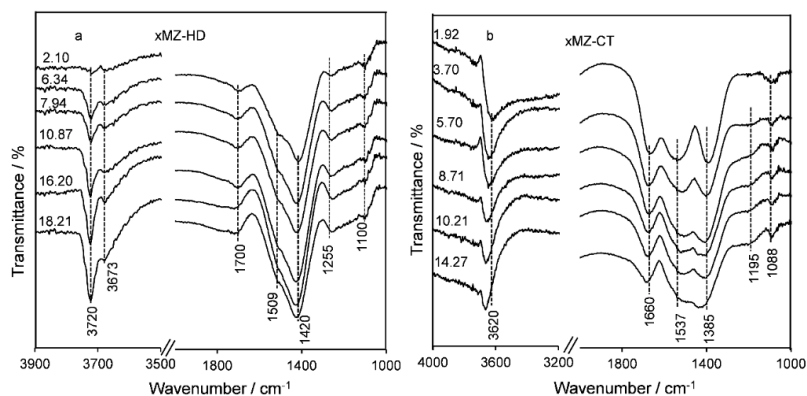
Figure 4. DRIFT spectra of: (**a**) xMZ–HD; and (**b**) xMZ–CT mixed oxides following subtraction of corresponding pure zirconia spectra.
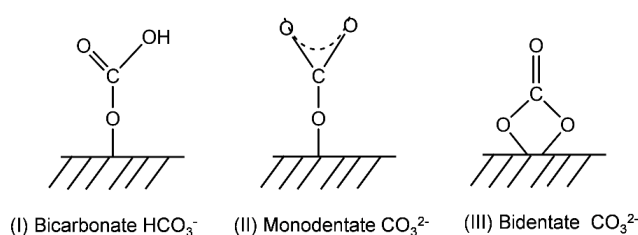

Scheme 2. Possible structure of surface carbonates.

Base strength was also assessed through CO_2-temperature-programmed desorption (TPD) measurements, with the resulting desorption profiles shown in Figure 5 and total basic site loadings presented in Table 1. All xMZ–HD samples exhibited an intense low temperature desorption with a maximum at ~100 °C attributed to CO_2 coordination to weak base sites such as hydroxyls, and a higher temperature desorption with a maximum at ~356 °C accompanied by a weaker shoulder at ~280 °C. The intensity of the high temperature features increased with MgO loading, being dominant for loadings ≥6.3 wt %, consistent with carbonate formation over strongly basic MgO crystallites. xMZ–CT samples show a qualitatively similar evolution of desorption spectra with MgO loading, being dominated by weak base sites (associated with a low temperature of ~100 °C desorption) for loadings <8.1 wt % wherein Mg is highly dispersed across zirconia, and strong base sites (associated with the 280–330 °C desorption) emerging at higher loadings due to MgO particle growth in accordance with DRIFTS.
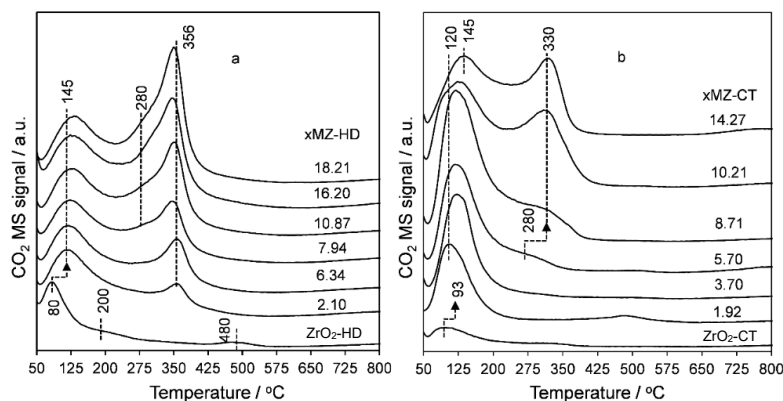
Figure 5. CO_2-temperature-programmed desorption (TPD) profiles of: (**a**) xMZ–HD; and (**b**) xMZ–CT mixed oxides.
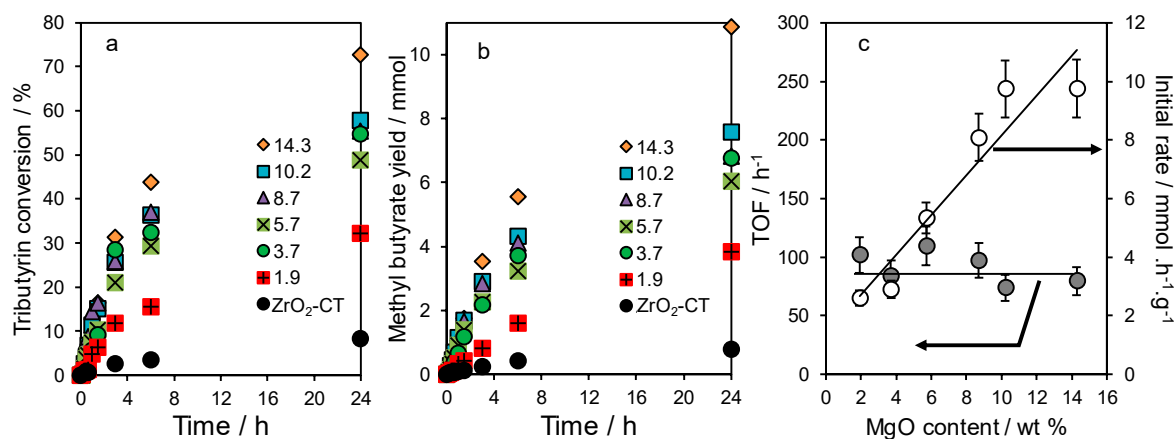
2.3. Tributyrin Transesterification

The impact of Mg incorporation on zirconia through the two synthetic routes on tributyrin transesterification with methanol is shown in Figures 6 and 7. Pure zirconia prepared by both routes was essentially inert, consistent with the low base site loadings in Table 1, and previous report of Kozlowski et al. [5]. Tributyrin conversion was significantly enhanced over both mixed oxide families, and proportional to the MgO content (Figures 6a and 7a), mirroring the total base site loading, and reached 85% and 75% over the 18.2MZ–HD and 14.3MZ–CT catalysts, respectively, after 24 h reaction at 63 °C. Methyl butyrate yields followed these trends (Figures 6b and 7b). Mass-normalized initial rates for the xMZ–HD catalysts rose linearly with MgO content (Figure 6c) to a maximum of ~10 mmol·g_{cat}^{-1}·h^{-1}, resulting in a constant turnover frequency (TOF, molecules of tributyrin converted per total base site per hour) of ~100 h^{-1} in excellent agreement with Kozlowski et al. [5]. The latter observation is indicative of a common, strong base MgO active site and consistent with DRIFTS which showed little variation in surface functionality across the family. Indeed, TOFs calculated per MgO strong base site for the MZ–HD family are quantitatively similar to those derived per total base site (Figure S7). Corresponding initial rates for the xMZ–CT catalysts are of comparable magnitude, and also show a linear increase with increasing MgO content. TOFs for the xMZ–CT family were approximately independent of MgO, and almost identical to those of xMZ–HD catalysts. Methyl butyrate selectivity at 20% iso-conversion was approximately independent of preparation route or MgO loading (Figure S8), further evidencing a common strongly basic MgO active site in all catalysts.
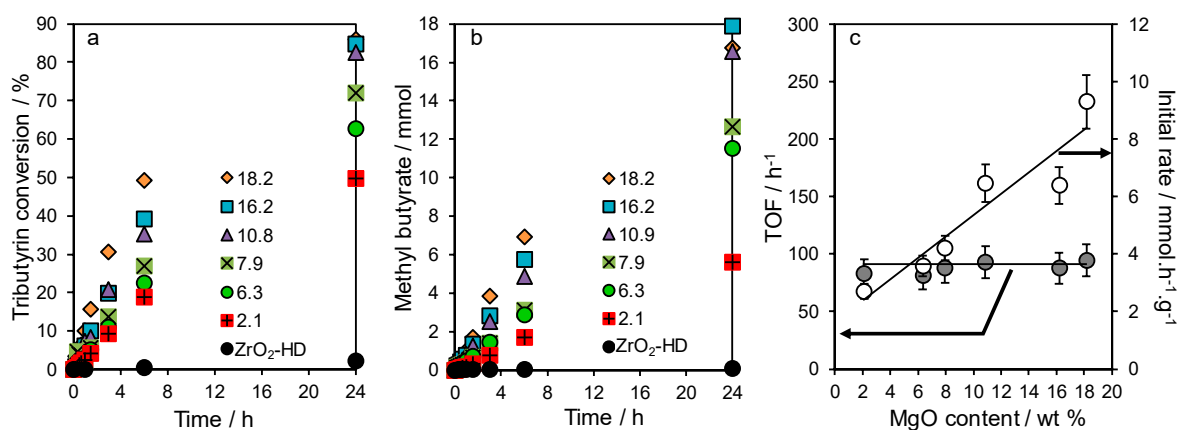

Figure 6. Tributyrin transesterification with methanol over xMZ–HD catalysts: (**a**) conversion; (**b**) methyl butyrate yield; and (**c**) mass-normalized initial rates and turnover frequency (TOF) per base site.

Figure 7. Tributyrin transesterification with methanol over xMZ–CT catalysts: (**a**) conversion; (**b**) methyl butyrate yield; and (**c**) mass-normalized initial rates and TOF per base site.

The reusability of the highest MgO loading 18.2MZ–HD and 1.43MZ–CT catalysts were subsequently studied over four consecutive reactions (three recycles). In both cases, monotonic decreases in both tributyrin conversion and selectivity to methyl butyrate of between 10% and 20% were observed (Figure 8). For the impregnated catalyst, this appears to correlate almost quantitatively with the homogeneous contribution identified through hot filtration due to MgO leaching (Table S2) during the first 1.5 h of reaction (Figure S9). The 14.3MZ–CT catalyst exhibited significant leaching (accounting for approximately one third of the observed tributyrin conversion in the first 24 h of the reaction), whereas the 18.2MZ–HD catalyst only underwent modest leaching, with a heterogeneous contribution of ~70% to the overall 86% tributyrin conversion after 24 h. In both cases, trace soluble $Mg(OCH_3)_2$ was also observed in the filtrate by IR spectroscopy (Figure S10). However, the (mid-loading) 8.7MZ–CT catalyst exhibited negligible leaching (Figure S11), with heterogeneous catalysis accounting for all of the observed 55% tributyrin conversion over 24 h. Note that both homogeneous and solid magnesium methoxide are reported to rapidly deactivate during this transesterification due to precipitation of butyric acid salts, resulting in low Turnover Numbers per Mg^{2+} [44]. Large MgO nanoparticles introduced either through the citrate-mediated route, or wet-impregnation thus contain a significant proportion of soluble Mg that leaches during transesterification. The wet-impregnated 18.2MZ–HD catalyst appears to reach steady state values of ~70% conversion and 55% selectivity to methyl butyrate after three consecutive reactions. In contrast, small MgO nanoparticles formed at lower loadings by the citrate route appear strongly coordinated to zirconia and/or possess higher MgO lattice enthalpies, and hence are extremely stable (and active) under our reaction conditions. After four consecutive reactions, the 14.3MZ–CT catalyst achieved 50% tributyrin conversion and ~40% selectivity to methyl butyrate, mirroring the (stable) performance of the lower loading 8.7MZ–CT sample, and hence, we suggest that irrespective of initial MgO loading, citrate prepared catalysts converge to a common steady state.
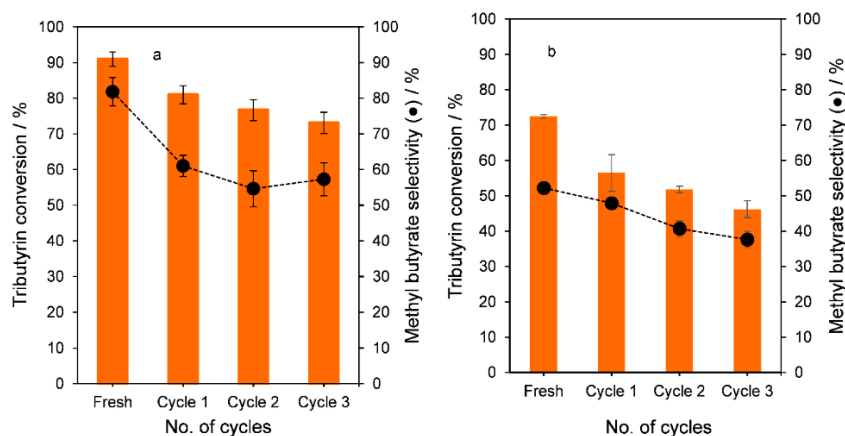
Figure 8. Tributyrin conversion and methyl butyrate selectivity as a function of recycle over: (**a**) 18.2MZ–HD; and (**b**) 14.3MZ–CT mixed oxide catalysts.

3. Experimental Details

3.1. Catalyst Synthesis

3.1.1. Non-Aqueous Impregnation

Mg–Zr mixed oxides (MZ), with nominal MgO contents in the range 3–20 wt %, were prepared by non-aqueous impregnation of $Zr(OH)_4$ (MEL Chemicals XZO 880/01) with magnesium methoxide solution (6–10 wt % in methanol, Aldrich 335657). Calculated volumes of the methoxide were added to 30 mL of anhydrous methanol (99.8% pure, Aldrich 322415) to which appropriate amounts of $Zr(OH)_4$ was slowly added. The resulting slurries were stirred at room temperature for 30 min under dry nitrogen, then heated at 65 °C until dry prior to calcination at 550 °C with a ramp rate of 5 °C·min^{-1} for 3 h in static air. The resulting materials are designated xMZ–HD, where x indicates the wt % MgO, and HD refers to the hydroxide precursor used.

3.1.2. Citrate-Mediated Sol–Gel

A second family of mixed oxide samples were prepared via citrate-mediated sol–gel processing with nominal MgO contents in the range 3–15 wt % according to methods found in the literature [33,45]. Appropriate quantities of zirconium oxychloride ($ZrOCl_2 \cdot 9H_2O$; 99% Research-Lab Fine Chem Industries 0161600100) and magnesium nitrate ($Mg(NO_3)_2 \cdot 6H_2O$; 98% Aldrich 237175) were dissolved in 100 mL of deionized water. One hundred mL of an aqueous citric acid ($C_6H_8O_7 \cdot H_2O$, 99% Aldrich C83155) solution was added to the mixed metal salt solution, with the citrate concentration equimolar to the total metal content, and the resulting mixture maintained at 85 °C until the solvent was almost fully evaporated. The obtained gel was dried at 200 °C, ground in an agate mortar, and then calcined at 550 °C with a ramp rate of 5 °C·min^{-1} for 3 h in static air. The resulting materials are designated xMZ–CT, where x indicates the wt % MgO, and CT refers to the citrate-mediated route.

3.2. Catalyst Characterization

Thermal analysis coupled with mass spectrometry was performed under flowing $N_2:O_2$ (2:1 volume ratio, 60 cm^3·min^{-1}) with a ramp rate of 10 °C min^{-1} using a Mettler-Toledo TGA/DSC2 thermal analyzer coupled to a Pfeiffer Thermostar mass spectrometer. Elemental analysis was performed using a ThermoScientific iCAP 7000 series analyzer on microwave-digested samples (CEM Discover SP-D microwave). N_2 porosimetry was undertaken at −195 °C on samples degassed overnight at 120 °C using a Quantachrome Nova 4200 porosimeter. Powder X-ray diffraction was performed using a Bruker D8 Advance diffractometer equipped with a LynxEye high-speed strip detector and Cu K$_\alpha$ (1.54 Å) radiation with a Ni filter and calibrated against a quartz

reference. Crystallite sizes were determined by X-ray line broadening from the Scherrer equation [46]. High resolution transmission electron microscopy (HR-TEM) was carried out on a JEOL 2100F FEG STEM operated at 200 keV on samples dispersed in methanol and drop cast onto a copper grid coated with a holey carbon support film (Agar Scientific Ltd., Essex, UK).

Diffuse Reflectance Infrared Fourier Transform (DRIFT) spectra were measured on a Thermo Scientific Nicolet iS50 FT-IR equipped with Smart Collector accessory, mid/near infrared source and mercury cadmium telluride (MCT) detector. Samples were diluted to 10 wt % in KBr powder, loaded into an environmental cell, and dried in vacuo at 50 °C for 10 min prior to analysis. X-ray photoelectron spectroscopy (XPS) was performed employing a Kratos Axis HSi spectrometer equipped with a charge neutralizer, monochromated Al K_α source (1486.7 eV), and a magnetic focusing lens. Spectra were recorded at normal emission using a pass energy of 40 eV under 1.3×10^{-9} Torr, with binding energies calibrated against adventitious carbon at 284.6 eV. Peak fitting was performed using CasaXPS version 2.3.15. Errors in XPS binding energies reflect the convolution of errors in the fitted peak position and the instrumental resolution of the monochromated Al X-ray source, which in combination give an accuracy of ~±0.2 eV. Temperature-programmed desorption (TPD) of CO_2 was undertaken using TGA–MS. Samples were degassed at 200 °C under flowing N_2 (10 mL·min^{-1}) overnight, then cooled to room temperature and exposed to flowing CO_2 (99.98% BOC) for 1 h. 20 mg (MZ–HD) or 60 mg (MZ–CT) of CO_2-saturated samples were then heated (ramp rate 10 °C·min^{-1}) to 900 °C under flowing N_2 (30 mL·min^{-1}) and the amount of CO_2 desorbed quantified by integration of the $m/z = 44$ mass channel, calibrated against $CaCO_3$.

3.3. Transesterification Activity

Transesterification was performed under stirred batch conditions at atmospheric pressure in a Radley's Carousel reaction station. Reactions were conducted using 10 mmol tributyrin (97% pure, Aldrich W222305) in 12.5 mL of methanol (MeOH:acid molar ratio = 30) at 63 °C, and 100 mg catalyst with 1.5 mmol dihexylether (97% pure, Aldrich 261505) as an internal standard. Reaction profiles were obtained via periodic sampling and analysis using a Shimadzu GC-2010 plus equipped with a ZB-50 capillary column (30 m × 0.32 mm × 0.25 μm), with each analysis performed in triplicate. Reactions were performed for 24 h, with initial rates determined from the linear portion of the conversion profile. Turnover frequencies (TOFs) were determined by normalizing initial rates to the total base site density determined from CO_2-TPD. Tributyrin conversion and selectivity to methyl butyrate were calculated as follows:

$$\text{Conversion (\%)} = \frac{[\text{Tributyrin}]_{t=0} - [\text{Tributyrin}]_t}{[\text{Tributyrin}]_{t=0}} \times 100$$

$$\text{Selectivity (\%)} = \frac{[\text{Methyl butyrate}]_t}{3 \times [\text{Tributyrin}]_{t=0}} \times 100$$

Catalyst recyclability was evaluated for three consecutive reactions: following 24 h reaction, the used catalyst was recovered by hot filtration, washed with methanol and anhydrous hexane, and added to a fresh reaction solution. Leaching was assessed by hot filtration after 1.5 h of reaction.

4. Conclusions

MgO–ZrO$_2$ mixed oxide catalysts were synthesized by either non-aqueous impregnation or citrate-mediated sol–gel routes. The selection of metal precursor and synthetic route had little impact on the resulting oxide phases formed post-calcination, which yielded c-MgO and t-ZrO$_2$, but influenced the MgO dispersion over the zirconia support; smaller MgO particles were obtained (for similar loadings) by the citrate-mediated sol–gel route. All catalysts exhibited weak Lewis acidity arising from the zirconia substrate, and strong Lewis basicity arising from the dispersed MgO nanoparticles. The initial rates and final conversion for tributyrin transesterification with methanol were directly proportional to the base site density (MgO loading), consistent with a common MgO

active site independent of the preparation or loading. High MgO concentrations, associated with large nanoparticles, were prone to partial leaching whether introduced by impregnation or sol–gel routes, however lower MgO loadings exhibited excellent stability. The latter observation suggests that improved transesterification performance requires the creation of high concentrations of small (<3 nm) MgO nanoparticles.

Supplementary Materials: The following are available online at http://www.mdpi.com/2073-4344/8/6/228/s1, Table S1. Elemental analysis of MZ catalysts prepared from hydroxide (MZ-HD) or citrate-mediated (MZ-CT) routes, Table S2. MgO mass loss from fresh 18.2MZ-HD catalyst as a function of recycle during tributyrin transesterification with methanol, Figure S1. (a) TGA/DTG, (b) DSC, and (c) MS signals for evolved gas species during thermal decomposition of $(CH_3O)_2Mg$-impregnated zirconium hydroxide precursor under flowing $N_2:O_2$ (2:1 volume ratio, 60 $cm^3 \cdot min^{-1}$), Figure S2. (a) TGA/DTG, (b) DSC, and (c) MS signals for evolved gas species during thermal decomposition of of citrate-mediated sol-gel under flowing $N_2:O_2$ (2:1 volume ratio, 60 $cm^3 \cdot min^{-1}$), Figure S3. Mg 2s XP spectra of (a) xMZ-HD, and (b) xMZ-CT mixed oxides, Figure S4. Zr 3d XP spectra of (a) xMZ-HD, and (b) xMZ-CT mixed oxides, Figure S5. O 1s XP spectra of (a) xMZ-HD, and (b) xMZ-CT mixed oxides, Figure S6. DRIFT spectra of (a) xMZ-HD, and (b) xMZ-CT mixed oxides, Figure S7. Comparison of TOF for tributyrin transesterification calculated per total base or per strong base (MgO) site, Figure S8. Methyl butyrate selectivity at 20% iso-conversion for metal oxides, Figure S9. Hot filtration tests to assess Mg^{2+} leaching in tributyrin transesterification over the indicated catalyst (catalyst was removed after 1.5 h), Figure S10. ATR-FTIR spectra of commercial magnesium methoxide solution and the supernatant post-reaction after 18.2MZ-HD catalyst, Figure S11. (a) Tributyrin conversion and methyl butyrate selectivity as a function of recycle, and (b) hot filtration tests to assess Mg^{2+} leaching over 8.7MZ-CT.

Author Contributions: Conceptualization, M.Z. and K.W.; Formal analysis, A.I.M.R., J.C.M., M.A.I., C.M.A.P., L.J.D. and A.F.L.; Investigation, A.I.M.R.; Methodology, A.I.M.R.; Supervision, M.I.Z. and K.W.; Writing original draft, A.I.M.R., M.I.Z., A.F.L. and K.W.; Writing review & editing, A.I.M.R. and A.F.L.

Conflicts of Interest: The authors declare no conflict of interest.

References

1. Gawande, M.B.; Pandey, R.K.; Jayaram, R.V. Role of mixed metal oxides in catalysis science—Versatile applications in organic synthesis. *Catal. Sci. Technol.* **2012**, *2*, 1113–1125. [CrossRef]

2. Aramendía, M.A.; Boráu, V.; Jiménez, C.; Marinas, J.M.; Marinas, A.; Porras, A.; Urbano, F.J. Synthesis and characterization of ZrO_2 as acid–basic catalysts: Reactivity of 2-methyl-3-butyn-2-ol. *J. Catal.* **1999**, *183*, 240–250. [CrossRef]

3. Tanabe, K.; Yamaguchi, T. Acid-base bifunctional catalysis by ZrO_2 and its mixed oxides. *Catal. Today* **1994**, *20*, 185–197. [CrossRef]

4. Komanoya, T.; Nakajima, K.; Kitano, M.; Hara, M. Synergistic Catalysis by Lewis Acid and Base Sites on ZrO_2 for Meerwein–Ponndorf–Verley Reduction. *J. Phys. Chem. C* **2015**, *119*, 26540–26546. [CrossRef]

5. Kozlowski, J.T.; Aronson, M.T.; Davis, R.J. Transesterification of tributyrin with methanol over basic Mg:Zr mixed oxide catalysts. *Appl. Catal. B Environ.* **2010**, *96*, 508–515. [CrossRef]

6. Liu, S.; Ma, J.; Guan, L.; Li, J.; Wei, W.; Sun, Y. Mesoporous CaO–ZrO_2 nano-oxides: A novel solid base with high activity and stability. *Microporous Mesoporous Mater.* **2009**, *117*, 466–471. [CrossRef]

7. Koirala, R.; Gunugunuri, K.R.; Pratsinis, S.E.; Smirniotis, P.G. Effect of zirconia doping on the structure and stability of CaO-based sorbents for CO_2 capture during extended operating cycles. *J. Phys. Chem. C* **2011**, *115*, 24804–24812. [CrossRef]

8. Wang, H.; Wang, M.; Zhao, N.; Wei, W.; Sun, Y. CaO–ZrO_2 solid solution: A highly stable catalyst for the synthesis of dimethyl carbonate from propylene carbonate and methanol. *Catal. Lett.* **2005**, *105*, 253–257. [CrossRef]

9. Gawande, M.B.; Branco, P.S.; Parghi, K.; Shrikhande, J.J.; Pandey, R.K.; Ghumman, C.; Bundaleski, N.; Teodoro, O.; Jayaram, R.V. Synthesis and characterization of versatile MgO–ZrO_2 mixed metal oxide nanoparticles and their applications. *Catal. Sci. Technol.* **2011**, *1*, 1653–1664. [CrossRef]

10. Faba, L.; Díaz, E.; Ordóñez, S. Gas phase acetone self-condensation over unsupported and supported Mg–Zr mixed-oxides catalysts. *Appl. Catal. B Environ.* **2013**, *142*, 387–395. [CrossRef]

11. Kozlowski, J.T.; Behrens, M.; Schlögl, R.; Davis, R.J. Influence of the Precipitation Method on Acid–Base-Catalyzed Reactions over Mg–Zr Mixed Oxides. *ChemCatChem* **2013**, *5*, 1989–1997. [CrossRef]

12. Sádaba, I.; Ojeda, M.; Mariscal, R.; Fierro, J.; Granados, M.L. Catalytic and structural properties of co-precipitated Mg–Zr mixed oxides for furfural valorization via aqueous aldol condensation with acetone. *Appl. Catal. B Environ.* **2011**, *101*, 638–648. [CrossRef]

13. Gawande, M.B.; Jayaram, R.V. A novel catalyst for the Knoevenagel condensation of aldehydes with malononitrile and ethyl cyanoacetate under solvent free conditions. *Catal. Commun.* **2006**, *7*, 931–935. [CrossRef]

14. Liu, S.; Zhang, X.; Li, J.; Zhao, N.; Wei, W.; Sun, Y. Preparation and application of stabilized mesoporous MgO–ZrO$_2$ solid base. *Catal. Commun.* **2008**, *9*, 1527–1532. [CrossRef]

15. Sree, R.; Babu, N.S.; Prasad, P.S.; Lingaiah, N. Transesterification of edible and non-edible oils over basic solid Mg/Zr catalysts. *Fuel Process. Technol.* **2009**, *90*, 152–157. [CrossRef]

16. Gawande, M.B.; Rathi, A.K.; Branco, P.S.; Potewar, T.M.; Velhinho, A.; Nogueira, I.D.; Tolstogouzov, A.; Ghumman, C.A.; Teodoro, O.M. Nano-MgO–ZrO$_2$ mixed metal oxides: Characterization by SIMS and application in the reduction of carbonyl compounds and in multicomponent reactions. *RSC Adv.* **2013**, *3*, 3611–3617. [CrossRef]

17. Wilson, K.; Hardacre, C.; Lee, A.F.; Montero, J.M.; Shellard, L. The application of calcined natural dolomitic rock as a solid base catalyst in triglyceride transesterification for biodiesel synthesis. *Green Chem.* **2008**, *10*, 654–659. [CrossRef]

18. Ma, F.; Hanna, M.A. Biodiesel production: A review1 Journal Series #12109, Agricultural Research Division, Institute of Agriculture and Natural Resources, University of Nebraska–Lincoln. 1. *Bioresour. Technol.* **1999**, *70*, 1–15. [CrossRef]

19. Gosch, B.J.; Magnusson, M.; Paul, N.A.; Nys, R. Total lipid and fatty acid composition of seaweeds for the selection of species for oil-based biofuel and bioproducts. *GCB Bioenergy* **2012**, *4*, 919–930. [CrossRef]

20. Carpenter, D.L.; Lehmann, J.; Mason, B.S.; Slover, H.T. Lipid composition of selected vegetable oils. *J. Am. Oil Chem. Soc.* **1976**, *53*, 713–718. [CrossRef]

21. Pinzi, S.; Garcia, I.L.; Lopez-Gimenez, F.J.; de Castro, M.D.L.; Dorado, G.; Dorado, M.P. The Ideal Vegetable Oil-based Biodiesel Composition: A Review of Social, Economical and Technical Implications. *Energy Fuels* **2009**, *23*, 2325–2341. [CrossRef]

22. Demirbas, A. Biodiesel from Vegetable Oils with MgO Catalytic Transesterification in Supercritical Methanol. *Energy Sources Part A Recover. Util. Environ. Eff.* **2008**, *30*, 1645–1651. [CrossRef]

23. Verziu, M.; Cojocaru, B.; Hu, J.; Richards, R.; Ciuculescu, C.; Filip, P.; Parvulescu, V.I. Sunflower and rapeseed oil transesterification to biodiesel over different nanocrystalline MgO catalysts. *Green Chem.* **2008**, *10*, 373–381. [CrossRef]

24. Gai, P.L.; Montero, J.M.; Lee, A.F.; Wilson, K.; Boyes, E.D. In situ Aberration Corrected-Transmission Electron Microscopy of Magnesium Oxide Nanocatalysts for Biodiesels. *Catal. Lett.* **2009**, *132*, 182–188. [CrossRef]

25. Montero, J.M.; Brown, D.R.; Gai, P.L.; Lee, A.F.; Wilson, K. In situ studies of structure–reactivity relations in biodiesel synthesis over nanocrystalline MgO. *Chem. Eng. J.* **2010**, *161*, 332–339. [CrossRef]

26. Montero, J.M.; Gai, P.; Wilson, K.; Lee, A.F. Structure-sensitive biodiesel synthesis over MgO nanocrystals. *Green Chem.* **2009**, *11*, 265–268. [CrossRef]

27. Man, I.-C.; Soriga, S.G.; Parvulescu, V. Theoretical aspects of methyl acetate and methanol activation on MgO (100) and (501) catalyst surfaces with application in FAME production. *Appl. Surf. Sci.* **2017**, *392*, 920–928. [CrossRef]

28. Lee, A.F.; Wilson, K. Recent developments in heterogeneous catalysis for the sustainable production of biodiesel. *Catal. Today* **2015**, *242*, 3–18. [CrossRef]

29. Jiang, D.-E.; Pan, G.; Zhao, B.; Ran, G.; Xie, Y.; Min, E. Preparation of ZrO$_2$-supported MgO with high surface area and its use in mercaptan oxidation of jet fuel. *Appl. Catal. A Gen.* **2000**, *201*, 169–176. [CrossRef]

30. Roehr, M.; Kubicek, C.P.; Komínek, J. Citric acid. In *Biotechnology Set*, 2nd ed.; John Wiley & Sons: Hoboken, NJ, USA, 2008; pp. 307–345.

31. Danks, A.; Hall, S.; Schnepp, Z. The evolution of 'sol–gel' chemistry as a technique for materials synthesis. *Mater. Horiz.* **2016**, *3*, 91–112. [CrossRef]

32. Lajavardi, M.; Kenney, D.J.; Lin, S.H. Time-Resolved Phase Transitions of the Nanocrystalline Cubic to Submicron Monoclinic Phase in Zirconia. *J. Chin. Chem. Soc.* **2000**, *47*, 1043–1053. [CrossRef]

33. Rabee, A.I.; Durndell, L.J.; Fouad, N.E.; Frattini, L.; Isaacs, M.A.; Lee, A.F.; Mekhemer, G.A.; dos Santos, V.C.; Wilson, K.; Zaki, M.I. Citrate-mediated sol–gel synthesis of Al-substituted sulfated zirconia catalysts for α-pinene isomerization. *Mol. Catal.* **2017**. [CrossRef]

34. Guo, X.; Mao, D.; Lu, G.; Wang, S.; Wu, G. CO$_2$ hydrogenation to methanol over Cu/ZnO/ZrO$_2$ catalysts prepared via a route of solid-state reaction. *Catal. Commun.* **2011**, *12*, 1095–1098. [CrossRef]

35. Nefedov, V.; Firsov, M.; Shaplygin, I. Electronic structures of MRhO$_2$, MRh$_2$O$_4$, RhMO$_4$ and Rh$_2$MO$_6$ on the basis of X-ray spectroscopy and ESCA data. *J. Electron Spectrosc. Relat. Phenom.* **1982**, *26*, 65–78. [CrossRef]

36. Barr, T.L. Recent advances in x-ray photoelectron spectroscopy studies of oxides. *J. Vac. Sci. Technol. A Vac. Surf. Films* **1991**, *9*, 1793–1805. [CrossRef]

37. Mekhemer, G.; Halawy, S.; Mohamed, M.; Zaki, M. Qualitative and quantitative assessments of acid and base sites exposed on polycrystalline MgO surfaces: Thermogravimetric, calorimetric, and in-situ FTIR spectroscopic study combination. *J. Phys. Chem. B* **2004**, *108*, 13379–13386. [CrossRef]

38. Lavalley, J. Infrared spectrometric studies of the surface basicity of metal oxides and zeolites using adsorbed probe molecules. *Catal. Today* **1996**, *27*, 377–401. [CrossRef]

39. Davydov, A. The Nature of Oxide Surface Centers. In *Molecular Spectroscopy of Oxide Catalyst Surfaces*; John Wiley & Sons, Ltd.: Hoboken, NJ, USA, 2003; pp. 27–179.

40. Busca, G.; Lorenzelli, V. Infrared spectroscopic identification of species arising from reactive adsorption of carbon oxides on metal oxide surfaces. *Mater. Chem.* **1982**, *7*, 89–126. [CrossRef]

41. León, M.; Díaz, E.; Bennici, S.; Vega, A.; Ordóñez, S.; Auroux, A. Adsorption of CO$_2$ on hydrotalcite-derived mixed oxides: Sorption mechanisms and consequences for adsorption irreversibility. *Ind. Eng. Chem. Res.* **2010**, *49*, 3663–3671. [CrossRef]

42. Debecker, D.P.; Gaigneaux, E.M.; Busca, G. Exploring, tuning, and exploiting the basicity of hydrotalcites for applications in heterogeneous catalysis. *Chem. A Eur. J.* **2009**, *15*, 3920–3935. [CrossRef] [PubMed]

43. Prinetto, F.; Ghiotti, G.; Durand, R.; Tichit, D. Investigation of acid–base properties of catalysts obtained from layered double hydroxides. *J. Phys. Chem. B* **2000**, *104*, 11117–11126. [CrossRef]

44. Martyanov, I.N.; Sayari, A. Comparative study of triglyceride transesterification in the presence of catalytic amounts of sodium, magnesium, and calcium methoxides. *Appl. Catal. A Gen.* **2008**, *339*, 45–52. [CrossRef]

45. Alifanti, M.; Baps, B.; Blangenois, N.; Naud, J.; Grange, P.; Delmon, B. Characterization of CeO$_2$−ZrO$_2$ mixed oxides. Comparison of the citrate and sol−gel preparation methods. *Chem. Mater.* **2003**, *15*, 395–403. [CrossRef]

46. Che, M.; Védrine, J.C. *Characterization of Solid Materials and Heterogeneous Catalysts: From Structure to Surface Reactivity*; John Wiley & Sons: Hoboken, NJ, USA, 2012.